The Astrophysical Journal Supplement Series, 265:26 (12pp), 2023 March https://doi.org/10.3847/1538-4365/acb705

Extended MCDHF Calculations of Energy Levels and Transition Data for N I

M. C. Li[1], W. Li[2], P. Jönsson[3], A. M. Amarsi[4], and J. Grumer[4]
[1] School of Electronic Information and Electrical Engineering, Huizhou University, Huizhou 516007, People's Republic of China
[2] National Astronomical Observatories, Chinese Academy of Sciences, Beijing 100012, People's Republic of China; wxli@nao.cas.cn
[3] Department of Materials Science and Applied Mathematics, Malmö University, SE-205 06 Malmö, Sweden
[4] Theoretical Astrophysics, Department of Physics and Astronomy, Uppsala University, Box 516, SE-751 20 Uppsala, Sweden
Received 2022 October 1; revised 2023 January 15; accepted 2023 January 23; published 2023 March 8

Abstract

Accurate and extensive atomic data are essential for spectroscopic analyses of stellar atmospheres and other astronomical objects. We present energy levels, lifetimes, and transition probabilities for neutral nitrogen, the sixth most abundant element in the cosmos. The calculations employ the fully relativistic multiconfiguration Dirac–Hartree–Fock and relativistic configuration interaction methods, and span the 103 lowest states up to and including $2s^22p^25s$. Our theoretical energies are in excellent agreement with the experimental data, with an average relative difference of 0.07%. In addition, our transition probabilities are in good agreement with available experimental and theoretical data. We further verify the agreement of our data with experimental results via a reanalysis of the solar nitrogen abundance, with the results from the Babushkin and Coulomb gauges consistent to 2% or 0.01 dex. We estimated the uncertainties of the computed transition data based on a statistical analysis of the differences between the transition rates in the Babushkin and Coulomb gauges. Out of the 1701 computed electric dipole transitions in this work, 83 (536) are associated with uncertainties smaller than 5% (10%).

Unified Astronomy Thesaurus concepts: Atomic data (2216); Solar abundances (1474)

Supporting material: machine-readable tables

1. Introduction

Nitrogen is the sixth most abundant element in the universe (Asplund et al. 2021), and its abundance is an important diagnostic in the study of the structure and evolution of stars (Hirschi 2007; Aerts et al. 2014; Maeder et al. 2014), globular clusters (Spite et al. 2022), and galaxies (Masseron & Gilmore 2015; Belfiore et al. 2017; Schiavon et al. 2017; Vincenzo & Kobayashi 2018; Esteban et al. 2020). Nitrogen abundance measurements in the atmospheres of stars via stellar spectroscopy are critical in this endeavor. In hot stars of spectral types O, B, A, and F, near-infrared and infrared N I lines arising from transitions involving the configurations $2p^2(^3P)3s$, $2p^2(^3P)3p$, $2p^2(^1D)3s$, $2p^2(^3P)3d$, and $2p^2(^1D)3p$ are typically used (Takeda & Takada-Hidai 1995; Przybilla & Butler 2001). Several weak N I lines can also be detected in cooler stars (Kolecki & Wang 2022), including the Sun; these have been used to inform the solar nitrogen abundance, together with molecular diagnostics such as NH and CN (Lambert 1978; Grevesse et al. 1990; Amarsi et al. 2020, 2021).

High-quality atomic data for N I are indispensable for reliable stellar spectroscopic analyses. During the past 30 yr, several dozen experimental and theoretical studies of transition data have been carried out for N I. The complete lists of published papers on these measurements and calculations can be retrieved from the NIST Atomic Transition Probability Bibliographic database (Kramida & Fuhr 2010). For example, on the experimental side, using a wall-stabilized arc source, measurements of transition probabilities and line strengths for visible and infrared lines, originating from transition arrays 3s–3p, 3s–4p, 3p–3d, and 4d–5s, were performed by Musielok et al. (1995), Bacławski et al. (2002), Bacławski & Musielok (2010, 2008), and Bridges & Wiese (2010). The relative uncertainties of these measurements were claimed to be no more than 15%. Using the same method, Goldbach & Nollez (1991) and Goldbach et al. (1992) measured the oscillator strengths for 19 lines in the 90–125 nm region and 18 lines in the 120–200 nm region, respectively. There are also a number of experimental measurements of lifetimes and oscillator strengths using various techniques (Dumont et al. 1974; Bromander et al. 1978; Catherinot & Sy 1979; Copeland et al. 1987; Bengtsson et al. 1992).

On the theoretical side, a few dozen theoretical studies of excitation energies and transition data for N I have been reported. For example, Hibbert et al. (1991) calculated the excitation energies and oscillator strengths for a number of dipole-allowed and intercombination transitions between doublet and quartet states with the configuration interaction method. Using the multiconfigurational Hartree–Fock and Breit–Pauli (MCHF-BP) method, calculations of oscillator strengths for N I have been performed by Tong et al. (1994), Tachiev & Froese Fischer (2002), and Froese Fischer & Tachiev (2004). Tong et al. (1994) only reported oscillator strengths of transitions among low-lying quartet states, whereas Tachiev & Froese Fischer (2002) and Froese Fischer & Tachiev (2004) calculated energy levels and lifetimes for all levels up to $2s^22p^23d$, as well as transition data between these levels. Among these theoretical results, the MCHF-BP values (Tachiev & Froese Fischer 2002; Froese Fischer & Tachiev 2004) are in overall better agreement with experimental results than the others. More recently, Bautista et al. (2022) calculated the *gf*-values of the two lines at 8683 Å and 8629 Å, which are diagnostics of the solar nitrogen abundance, using a combination of different methods, i.e., AUTOSTRUCTURE based on the Thomas–Fermi–Dirac–Amaldi central potential, pseudorelativistic

Hartree–Fock, and multiconfiguration Dirac–Hartree–Fock (MCDHF) methods.

In the present work, we perform large-scale ab initio calculations of excitation energies and electric dipole (E1) transition parameters (transition rates, line strengths, and weighted oscillator strengths) for the 103 lowest states belonging to the $2s^22p^3$, $2s2p^4$, $2s^22p^2nl$ ($n = 3, 4$, $l =$ s, p, d, f), and $2s^22p^25s$ configurations in N I. Calculations are based on fully relativistic MCDHF and configuration interaction (RCI) methods, as implemented in the general-purpose relativistic atomic structure package GRASP2018[5] (Froese Fischer et al. 2019).

2. Theory and Computations

2.1. Theory

In the MCDHF method (Froese Fischer et al. 2016) as implemented in the GRASP code, the atomic eigenstate is represented by an atomic state expressed as a linear combination of configuration state functions (CSFs) with equal parity P and angular momentum quantum numbers JM,

$$\Psi(\gamma PJM) = \sum_i c_i \Phi(\gamma_i PJM). \quad (1)$$

The CSFs are jj-coupled many-electron functions built from antisymmetrized products of single-electron Dirac orbitals. The quantities c_i and γ_i are the mixing coefficient and additional labeling, respectively, needed to uniquely specify each CSF. The radial parts of the Dirac orbitals and the expansion coefficients c_i of the targeted states are all optimized to self-consistency by solving the MCDHF equations, which are derived by applying the variational principle on the weighted average energy of the targeted states. Higher-order electron-electron interactions, such as the frequency-independent Breit interaction and leading quantum electrodynamical effects in the form of the self-energy (SE) and the screened vacuum polarization (VP), are included in the subsequent RCI calculations using the orbital basis from the MCDHF optimization (Grant 2007).

The E1 transition data (transition probabilities and weighted oscillator strengths) between two states $\gamma' P' J'$ and γPJ are expressed in terms of reduced matrix elements of the electric dipole transition operator $T^{(1)}$. From Equation (1), these matrix elements can be written as

$$\langle \Psi(\gamma PJ) \| T^{(1)} \| \Psi(\gamma' P' J') \rangle = \sum_{i,j} c_i c_j' \langle \Phi(\gamma_i PJ) \| T^{(1)} \| \Phi(\gamma_j' P' J') \rangle. \quad (2)$$

Here, c_i and c_j are the expansion coefficients of the CSFs for the upper and lower states, respectively. Using the Brink and Satchler convention, the reduced matrix elements in Equation (2) can be expressed in terms of spin-angular coefficients $d_{ab}^{(1)}$ and operator strengths as

$$\langle \Phi(\gamma_i PJ) \| T^{(1)} \| \Phi(\gamma_j' P' J') \rangle = \sum_{a,b} d_{ab}^{(1)} \langle n_a l_a j_a \| t^{(1)} \| n_b l_b j_b \rangle, \quad (3)$$

[5] See also the open-source GitHub repository maintained by the CompAS collaboration: https://github.com/compas/grasp.

Table 1
Summary of the Active Space Construction

Parity	MR	Extended MR in RCI	$N_{\rm CSFs}$
Even	$2s2p^4$, $2s^22p^23s$ $2s^22p^23d$, $2s^22p^24s$ $2s^22p^24d$, $2s^22p^25s$	$2s2p^3np(3 \leqslant n \leqslant 5)$ $2p^4nl(3 \leqslant n \leqslant 5, l =$ s, d)	13,431,751
Odd	$2s^22p^3$, $2s^22p^23p$ $2s^22p^24p$, $2s^22p^24f$	$2s2p^3nl(3 \leqslant n \leqslant 5, l =$ s, d) $2p^44f$, $2s2p^4np(3 \leqslant n \leqslant 5)$	17,662,086

Note. The configurations in the second and third columns represent the target states and the extended target MR set in RCI calculation, respectively. $N_{\rm CSFs}$ denotes the number of CSFs in the total expansion for the even and odd parity states in the final RCI calculation.

where

$$\langle n_a l_a j_a \| t^{(1)} \| n_b l_b j_b \rangle = \left(\frac{(2j_b + 1)\omega}{\pi c} \right)^{1/2} (-1)^{j_a - 1/2} \begin{pmatrix} j_a & 1 & j_b \\ \frac{1}{2} & 0 & -\frac{1}{2} \end{pmatrix} \overline{M_{ab}}. \quad (4)$$

Here, n, l, j are the principal, orbital, and angular quantum numbers of spin orbitals a and b, respectively, $\hbar\omega$ is the electromagnetic energy, and $\overline{M_{ab}}$ is the radiative transition integral defined by Grant (1974). For electric type multipoles, the $\overline{M_{ab}}$ integral can be written as $\overline{M_{ab}}(G) = \overline{M_{ab}^e} + G\overline{M_{ab}^l}$ (see Equation (4).10 in Grant 1974), where $\overline{M_{ab}^e}$ is the Coulomb gauge integral , $\overline{M_{ab}^l}$ is the longitudinal part, and G is the gauge parameter. Two familiar choices, corresponding to the velocity and length operator forms in nonrelativistic theory, are the Coulomb ($G = 0$) and Babushkin ($G = \sqrt{2}$) gauges.

The agreement between transition rates in the Coulomb gauge ($A_{\rm C}$) and the Babushkin gauge ($A_{\rm B}$) is often taken as an internal indicator of accuracy of calculated data, especially when no experimental results are available. The relative differences between transition rates $A_{\rm B}$ and $A_{\rm C}$, dT, is defined as (Froese Fischer 2009; Ekman et al. 2014)

$$dT = \frac{|A_{\rm B} - A_{\rm C}|}{\max(A_{\rm B}, A_{\rm C})}. \quad (5)$$

It should be emphasized that dT gives an estimation of the uncertainty for groups of lines in a statistical manner.

2.2. Computational Schemes

Calculations were performed in the extended optimal level scheme (Dyall et al. 1989) for the weighted average of the even and odd parity states. These states belong to the $\{2s2p^4, 2s^22p^2nl(n = 3, 4, l =$ s, d), $2s^22p^25s\}$ even configurations and the $\{2s^22p^3, 2s^22p^2nl(n = 3, 4, l =$ p, f)$\}$ odd configurations. These target configurations are included in the multireference (MR) set used in the MCDHF calculations.

Following the CSF generation strategies used by, e.g., Papoulia et al. (2019) and Li et al. (2021), the MCDHF calculations were based on CSF expansions for which we impose restrictions on the orbital excitations from the deeper subshells. The CSFs are generated and systematically enlarged through single and double (SD) excitation from subshells occupied in the predefined MR configurations to an active set of orbitals in a step-by-step manner (Olsen et al. 1988; Sturesson et al. 2007; Froese Fischer et al. 2016).

Table 2
Energies (in cm^{-1}) and Lifetimes (in Seconds) in Both the Babushkin (τ_B) and Coulomb (τ_C) Gauges for the Lowest 103 Levels of N I

No.	State	*LS*-composition	E_{RCI}	E_{NIST}	ΔE	τ_B	τ_C
1	$2s^22p^3\ ^4S^o_{3/2}$	0.91	0	0.000	0		
2	$2s^22p^3\ ^2D^o_{5/2}$	0.89	19426	19224.464	−201		
3	$2s^22p^3\ ^2D^o_{3/2}$	0.89	19435	19233.177	−201		
4	$2s^22p^3\ ^2P^o_{1/2}$	$0.85 + 0.03\ 2p^5\ ^2P^o$	29142	28838.920	−304		
5	$2s^22p^3\ ^2P^o_{3/2}$	$0.85 + 0.03\ 2p^5\ ^2P^o$	29143	28839.306	−303		
6	$2s^22p^2(^3P)3s^4P_{1/2}$	$0.82 + 0.12\ 2s2p^4\ ^4P$	83332	83284.070	−48	2.44E-09	2.44E-09
7	$2s^22p^2(^3P)3s^4P_{3/2}$	$0.82 + 0.12\ 2s2p^4\ ^4P$	83366	83317.830	−48	2.42E-09	2.42E-09
8	$2s^22p^2(^3P)3s^4P_{5/2}$	$0.81 + 0.12\ 2s2p^4\ ^4P$	83413	83364.620	−49	2.40E-09	2.39E-09
9	$2s^22p^2(^3P)3s^2P_{1/2}$	0.95	86187	86137.350	−50	2.10E-09	2.10E-09
10	$2s^22p^2(^3P)3s^2P_{3/2}$	0.95	86270	86220.510	−50	2.10E-09	2.10E-09

Note. Energy levels are given relative to the ground state and compared with results from NIST-ASD (Kramida et al. 2021). The labeling in the second column is defined by the composition with the largest expansion coefficient given in the third column. The third column gives the wave function composition (up to three *LS*-components with a fractional contribution of >0.02 of the total wave function) in *LS*-coupling. ΔE donates the differences between the MCDHF/RCI calculated values and the compiled values from NIST-ASD, i.e., $\Delta E = E_{NIST} - E_{RCI}$. Note that the labeling of the two level pairs, 74–75 and 80–82, given in the second column, is inverted compared to that of the NIST-ASD data.

(This table is available in its entirety in machine-readable form.)

In our calculations, the orbitals in the $n = 1$ shell of the MR configurations are defined as core orbitals. The remaining orbitals are defined as valence orbitals. Based on these definitions, the valence–valence electron correlations are included in the calculation by allowing SD excitations from the valence orbitals to active sets of orbitals, with the restriction that there is one excitation from the $n = 2$ shell at most.

With an MCDHF orbital basis at hand, the MR set was then further extended and applied in a subsequent RCI calculation, as shown in Table 1. The extended MR set comprises configurations that give rise to *LSJ*-coupled CSFs with weights larger than 0.05. Core–valence electron correlation effects were taken into account by allowing SD substitutions from the valence shells and the $1s^2$ core of the configurations in the extended MR, with the restriction that one excitation is allowed from $1s^2$ to the final active set {11s, 10p, 10d, 10f, 7g, 6h} at most. The numbers of CSFs in the final even and odd state expansions were 13,431,751 and 17,662,086, respectively, distributed over the different *J* symmetries.

3. Results and Discussion

3.1. Energies and Lifetimes

The calculated energies and corresponding wave function composition in *LS*-coupling for the lowest 103 states are displayed in Table 2. The labeling of the eigenstates is defined by the *LSJ*-coupled CSF with the largest expansion coefficient, resulting from the transformation from *jj*-coupling to *LSJ*-coupling using the method by Gaigalas et al. (2017). We note that *LSJ*-coupling might not be the best representation to describe the states associated with the $2s^22p^24f$ configuration and that the National Institute of Standards and Technology Atomic Spectra Database (NIST-ASD; Kramida et al. 2021) adopts *JK*-coupling in their labeling of these. The corresponding experimental energies provided via NIST-ASD, as well as radiative lifetimes in both Babushkin (B) and Coulomb (C) forms are also included in Table 2. When compared with energies from NIST-ASD, we realized that two pairs of levels, 74–75 ($2p^24d\ ^4P_{5/2}$ and $^2F_{5/2}$) and 80–82 ($2p^24d\ ^4D_{1/2}$ and $^4P_{1/2}$), were inverted based on the energy ordering. A closer inspection of the *LS*-composition reveals that these states are strongly mixed, the leading percentages being about 40%–60% and the second components about 30%–40%, and they might be less accurately described by the conventional labeling based on the expansion coefficients. Since a close agreement of the computed energies with the NIST-ASD values is observed for the other levels, we matched the corresponding two pairs of levels with experimental energies based on the energy ordering within each symmetry. Note that the labeling of these two pairs of levels, i.e., 74–75 and 80–82, given in the second column of Table 2, is inverted compared to that of the NIST-ASD data.

The results of the comparison of the computed energy levels in this work with experimental values are shown in Figure 1. As seen in the left panel of Figure 1, our computed energies agree very well with the NIST-compiled experimental energies with an average relative difference of 0.07%. The largest relative difference between theory and experiment is 1.05% for the levels belonging to doublet terms of the $2s^22p^3$ ground configuration. For the remaining 98 levels, the relative differences of the computed excitation energies are much smaller, with an average of 0.03%. The right panel of Figure 1 shows the energy differences between NIST-ASD values and our computed data, $\Delta E = E_{NIST}E_{RCI}$, plotted against the excitation energies, E_{RCI}. We can see that the largest error occurs for the ground levels, which are about 200–300 cm^{-1} higher than the NIST-ASD values. The rms of the ΔE values is about 67 cm^{-1}. When the computational excitation energies are corrected with the linear fitting results, the rms of the ΔE values decreased to 28 cm^{-1}, with a systematic error of 0.26% of the excitation energies.

In Table 3 we compare the lifetimes from our calculations with other theoretical results and experimental values, when available. The calculated lifetimes in the Babuskin and Coulomb forms are in agreement within 2.6%. Compared with the theoretical results from the CIV3 calculations by Hibbert et al. (1991) and the MCHF-BP calculations by Froese Fischer & Tachiev (2004), excellent agreement is observed for seven out of eight lifetime values, with the relative difference between two of them each being smaller than 7%. For the $2p^2(^3P)4s^2P$ term, the lifetime value from our work is about a factor of two smaller than the CIV3 results, but in agreement with the MCHF-BP value, with the relative difference smaller

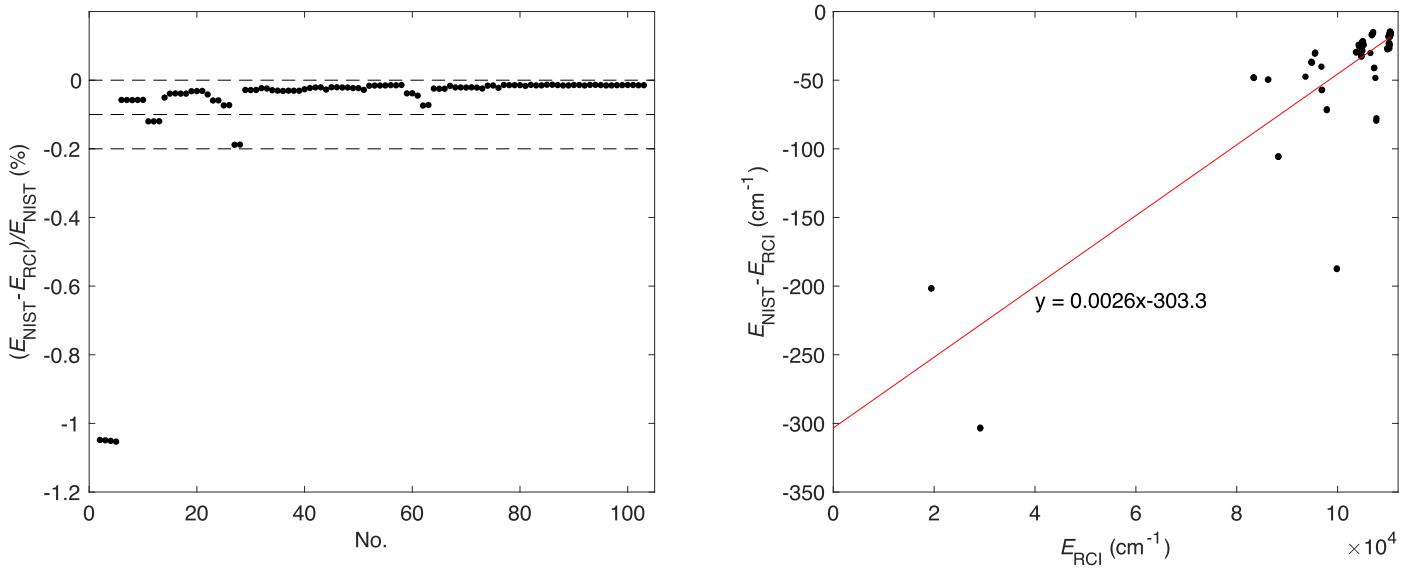

Figure 1. Comparison of the current computed excitation energies with the values available in the NIST-ASD. The left panel shows the relative difference for each level, and the right panel shows the absolute difference along with the energies computed by us. The dashed lines in the left panel, from the upper to the lower panel, indicate the 0.2%, 0.1%, and 0.0% relative discrepancies, respectively. The solid red line in the right panel is the linear fit to the scatter data shown in the figure.

Table 3
Comparison of the Experimental and Calculated Lifetimes (in Nanoseconds; B = Babuskin Form and C = Coulomb Form)

State or Term	This Work		Other Calculations	Experiments
	B	C		
$2p^2(^3P)3p\ ^4D_{7/2}$	39.8	40.3	37.9[a]; 37.12[b]	44(2)[c]; 43(3)[d]
$2p^2(^3P)3p\ ^4S_{3/2}$	25.3	25.5	24.1[a]; 23.26[b]	26.0(1.5)[c]; 23.3(2.3)[e]
$2p^2(^3P)3p\ ^4P_{5/2}$	33.4	33.9	31.6[a]; 31.22[b]	39[f]; 55(5)[g]
$2s2p^4\ ^4P$	6.90	6.75	6.77[a]; 7.14[b]	7.3(0.7)[h]; 7.4(0.4)[i]; 7.0(0.2)[j] 7.1(0.4)[f];5.5(1.5)[k], 9.9(1.0)[l]; 7.2(0.7)[m]
$2p^2(^3P)3s\ ^4P$	2.42	2.42	2.48[a]; 2.59[b]	2.35(0.23)[f,h]; 2.4(0.1)[j]; 2.2(0.4)[l]; 2.5(0.3)[m]
$2p^2(^3P)3s\ ^2P$	2.10	2.10	2.13[a]; 1.95[b]	1.9(0.3)[h,m]; 2.3(0.4)[h]; 2.2(0.1)[j] 1.7(0.4)[l]; 1.9(0.4)[l]; 2.28(0.2)[f]
$2p^2(^1D)3s\ ^2D$	2.57	2.58	2.44[a]; 2.44[b]	2.27(0.3)[h]; 2.26(0.3)[h]; 2.65(0.3)[f] 2.6(0.1)[j]; 2.5(0.4)[k]; 2.2(0.3)[m]
$2p^2(^3P)4s\ ^2P$	8.52	8.75	8.02[a]; 18.8[b]	6.2[h]

Notes. The lifetime of a term is the mean value of the lifetime corresponding to the different J values. The notation for experimental values, e.g., 44(2), implies 44 ± 2.
[a] Froese Fischer & Tachiev (2004).
[b] Hibbert et al. (1991).
[c] Bengtsson et al. (1992).
[d] Copeland et al. (1987).
[e] Catherinot & Sy (1979).
[f] Désesquelles (1970).
[g] Bromander et al. (1978).
[h] Dumont et al. (1974).
[i] Smith et al. (1970).
[j] Berry et al. (1971).
[k] Mallow & Burns (1972).
[l] Hutchison (1971).
[m] Lawrence & Savage (1966).

than 6%, and it is in better agreement with the experimental value from Dumont et al. (1974). Good agreement is also observed between computed and experimental lifetime values, except for the $2p^2(^3P)3p^4P^o_{5/2}$ and $2p^2(^3P)4s^2P$ levels. For the $2p^2(^3P)3p^4P^o_{5/2}$ level, all the theoretical lifetimes differ substantially from the experimental values, and the two experimental values by Bromander et al. (1978) and Désesquelles (1970) differ by 30% with each other. In contrast, the theoretical results obtained from three different methods, i.e., MCDHF, MCHF-BP, and CIV3, are in good agreement within 8%. For the $2p^2(^3P)4s^2P$ state, all the theoretical values are higher than the experimental result obtained from Dumont et al. (1974). Our predicted lifetime is in good agreement with that from the MCHF-BP calculation (Froese Fischer & Tachiev 2004), while

Table 4
Electric Dipole Transition Data for N I from Our Calculations

Upper	Lower	λ (Å)	A_B (s^{-1})	A_C (s^{-1})	$\log(gf)_B$	$\log(gf)_C$	S_B	S_C	dT	Acc.	
										dT and A	gf_{RCI} and $gf_{NIST-ASD}$
$2s^2\ 2p^2\ (^3P)\ 4d\ ^2D_{5/2}$	$2s^2\ 2p^3\ ^4S^o_{3/2}$	905.221	1.444E+06	1.623E+06	−2.973	−2.922	3.172E-03	3.565E-03	0.110	C+	C
$2s^2\ 2p^2\ (^3P)\ 4d\ ^2D_{3/2}$	$2s^2\ 2p^3\ ^4S^o_{3/2}$	905.411	4.649E+05	5.202E+05	−3.641	−3.592	6.813E-04	7.623E-04	0.106	C+	D+
$2s^2\ 2p^2\ (^3P)\ 4d\ ^4D_{5/2}$	$2s^2\ 2p^3\ ^4S^o_{3/2}$	905.786	1.657E+07	1.861E+07	−1.913	−1.862	3.647E-02	4.096E-02	0.110	C+	B
$2s^2 2p^2\ (^3P)\ 4d\ ^4D_{3/2}$	$2s^2\ 2p^3\ ^4S^o_{3/2}$	905.834	3.476E+07	3.898E+07	−1.767	−1.717	5.101E-02	5.719E-02	0.108	C+	B
$2s^2\ 2p^2\ (^3P)\ 4d\ ^4P_{1/2}$	$2s^2\ 2p^3\ ^4S^o_{3/2}$	905.914	5.361E+07	6.005E+07	−1.880	−1.830	3.935E-02	4.407E-02	0.107	C+	B
$2s^2\ 2p^2\ (^3P)\ 4d\ ^4D_{1/2}$	$2s^2\ 2p^3\ ^4S^o_{3/2}$	906.207	3.201E+07	3.588E+07	−2.103	−2.054	2.352E-02	2.636E-02	0.108	C+	C+
$2s^2\ 2p^2\ (^3P)\ 4d\ ^4P_{3/2}$	$2s^2\ 2p^3\ ^4S^o_{3/2}$	906.432	4.903E+07	5.510E+07	−1.617	−1.566	7.209E-02	8.101E-02	0.110	C+	B
$2s^2 2p^2\ (^3P)\ 4d\ ^2F_{5/2}$	$2s^2\ 2p^3\ ^4S^o_{3/2}$	906.619	2.562E+07	2.893E+07	−1.722	−1.670	5.655E-02	6.385E-02	0.114	C+	B
$2s^2\ 2p^2\ (^3P)\ 4d\ ^4P_{5/2}$	$2s^2\ 2p^3\ ^4S^o_{3/2}$	906.731	3.759E+07	4.248E+07	−1.556	−1.503	8.298E-02	9.377E-02	0.115	C+	B
$2s^2\ 2p^2\ (^3P)\ 4d\ ^2P_{1/2}$	$2s^2\ 2p^3\ ^4S^o_{3/2}$	907.069	1.240E+06	1.416E+06	−3.514	−3.457	9.139E-04	1.043E-03	0.124	C+	D+

Note. Upper and lower states, wavelength in vacuum, $\lambda_{vac.}$, transition probability, A, line strength, S (in atomic units of $a_0^2 e^2$), weighted oscillator strength, $\log(gf)$, together with the relative difference between two gauges of A values, dT, and Accuracy class, Acc., are shown in the table. The wavelengths and all the transition parameters are adjusted to the NIST-ASD Ritz wavelength values. The accuracy class, Acc., is given by A (Uncertainty $\leqslant$3%), B+ (3% < Uncertainty $\leqslant$7%), B (7% < Uncertainty $\leqslant$10%), C+ (10% < Uncertainty $\leqslant$18%), C (18% < Uncertainty $\leqslant$25%), D+ (25% < Uncertainty $\leqslant$40%), D (40% < Uncertainty $\leqslant$50%), and E (50% > Uncertainty). A_B, $\log(gf)_B$, and S_B are the transition rates, weighted oscillator strengths, and line strengths in the Babushkin (B) form, respectively. A_C, $\log(gf)_C$, and S_C are the transition rates, weighted oscillator strengths, and line strengths in the Coulomb (C) form, respectively.

(This table is available in its entirety in machine-readable form.)

Table 5
Statistical Results of dT for the Computed Transition Rates

Group	No.	$\langle dT\rangle$	σ
$<10^0$	68	65.77	0.35
$10^0 - 10^2$	199	26.65	0.25
$10^2 - 10^4$	422	17.70	0.20
$10^4 - 10^6$	670	9.42	0.12
$>10^6$	342	4.51	0.08
$dT < 20$		84.31	
$dT < 10$		66.04	
$dT < 5$		51.74	

Note. The transitions are divided into five groups based on the magnitude of the A values (in s^{-1}). The number of transitions (No.), the mean dT ($\langle dT\rangle$), and the standard deviations (σ) are given for each group of the transitions. The last three rows show the proportions (in percent) of the transitions with dT lower than 0.2, 0.1, and 0.05 in all the transitions with $A \geqslant 10^2$ s^{-1}.

the value from Hibbert et al. (1991) is higher than the others. New experimental measurements of lifetimes would therefore be welcome for these levels.

3.2. Transition Parameters

The E1 transition data, such as wavelengths (λ), transition rates (A), line strengths (S), and weighted oscillator strengths (gf) in Babushkin gauge, are listed in Table 4. We note that the wavelengths in Table 4 are computed from the experimental energy levels compiled in NIST-ASD, and the transition parameters A and gf are also adjusted to the NIST-ASD wavelength values.

As mentioned in Section 2.1, the dT values can be used to assess the accuracy of the transition parameters. The former are shown in the last column of Table 4. We also investigated the distribution of dT values with respect to the magnitude of the transition rates A. In Table 5, the transitions are organized in five groups based on the magnitude of the A values and the statistical results of dT values, i.e., the mean value $\langle dT\rangle$ and the corresponding standard deviations σ, are given for each group. $\langle dT\rangle$ and σ are defined as

$$\langle dT\rangle = \frac{\sum_{i=1}^{n} dT_i}{n} \tag{6}$$

$$\sigma = \sqrt{\frac{\sum_{i=1}^{n}(dT_i - \langle dT\rangle)^2}{(n-1)}}, \tag{7}$$

where n is the number of transitions of each group.

As can be seen from Table 5, stronger transitions are usually associated with lower dT values, while weaker transitions are associated with relatively higher dT values. This is expected because these weaker transitions are mainly unexpected, LS-forbidden E1 transitions, for example, the intercombination transitions and two-electron one-photon transitions, and the challenging nature involved in the computations of these types of transitions due to extensive cancellation between large contributions, see e.g., Ynnerman & Froese Fischer (1995). The cancellation effect can be represented by the cancellation factor (CF). Computed line strengths are expected to show large uncertainties when CF is smaller than about 0.1 or 0.05 (Cowan 1981). For the LS-allowed transitions computed in this work, 537 out of 905 transitions are associated with CFs larger than 0.05, but the CFs are larger for only 167 out of 796

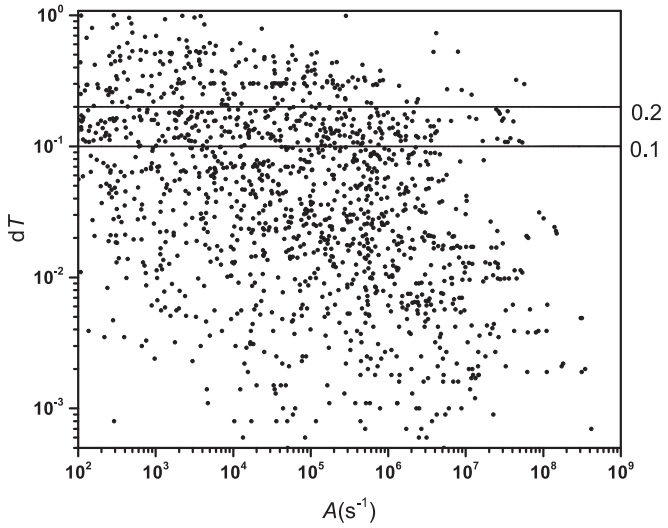

Figure 2. Distributions of dT values along with transition rates A in s^{-1}. The solid lines indicate the 0.1 and 0.2 relative difference between the Babuskin and Coulomb gauges. Note that a logarithmic scale is used in both the x- and y-axes.

transitions for LS-forbidden transitions. For most of the strong transitions with $A > 10^6$ s^{-1}, the mean $\langle dT\rangle$ is smaller than 0.05 ($\sigma = 0.08$). The proportions of the transitions with different dT values are also statistically analyzed and shown in the last three rows: they are 84.3%, 66.0%, and 51.7% for transitions with dT smaller than 0.2, 0.1, and 0.05, respectively.

Figure 2 depicts the distributions of the dT values for all the E1 transitions with $A > 10^2$ s^{-1}. The distribution is consistent with the finding in Table 5 that stronger transitions are associated with lower dT values and that the dT values are within 0.2 for most of the transitions. The mean dT for all presented E1 transitions shown in Figure 2 is 0.107 ($\sigma = 0.18$).

However, the estimation of uncertainties for each transitions is not trivial, and a number of methods have been proposed for the estimation of the uncertainties of the calculated transition rates (Froese Fischer 2009; Ekman et al. 2014; Kramida 2014; Gaigalas et al. 2020; El-Sayed 2021). In this work, the estimation of the uncertainty is performed by two methods. The first method, which we call the dT and A procedure, is performed in steps as follows: 1. The transitions are divided into groups based on the A values, i.e., $A < 10^0$ s^{-1}, $10^0 \leqslant A < 10^2$ s^{-1}, $10^2 \leqslant A < 10^3$ s^{-1}, $10^3 \leqslant A < 10^4$ s^{-1}, $10^4 \leqslant A < 10^5$ s^{-1}, $10^5 \leqslant A < 10^7$ s^{-1}, and $A \geqslant 10^7$ s^{-1}. 2. The averaged $dT_{\rm av}$ is determined for each group. 3. The related uncertainty percentage for each transition equals $\max(dT, dT_{\rm av})$. The second method employs the procedure from Kramida (2013), which evaluates the accuracy of the computed transition probabilities from a comparison of $gf_{\rm RCI}$ and the results from NIST-ASD, $gf_{\rm NIST-ASD}$, and we call it the $gf_{\rm RCI}$ and $gf_{\rm NIST-ASD}$ method. The statistical analysis of the number of transitions belonging to specific accuracy classes is performed, and the percentage fractions obtained from the above two methods are shown in Figure 3.

For comparison, the percentage fractions in different uncertainty categories obtained from dT values are also shown in Figure 3. We can see that the percentage fraction belonging to the high-accuracy class decreases from 45% when the dT indicator is used to 5% using the dT and A procedure and 0 using the $gf_{\rm RCI}$ and $gf_{\rm NIST-ASD}$ method, which indicates that using the dT values only for accuracy estimations might

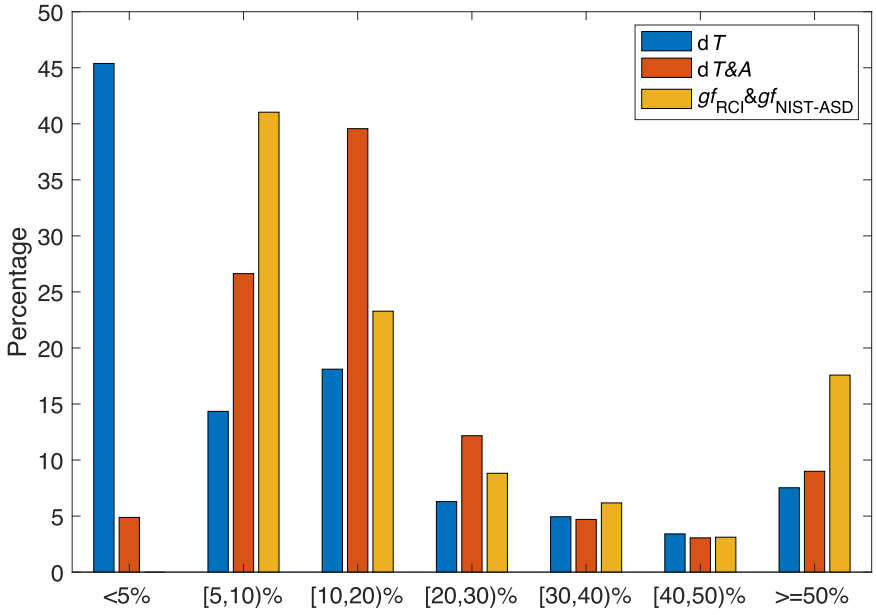

Figure 3. Percentage fractions of all transitions in different uncertainty categories for the uncertainties based on dT values alone (blue), based on the $dT\&A$ procedure (red), and based on the $gf_{\rm RCI}$ and $gf_{\rm NIST-ASD}$ method (yellow) of Kramida (2013).

underestimate the uncertainties. The accuracy classes obtained from dT and A and $gf_{\rm RCI}$ and $gf_{\rm NIST-ASD}$ methods are given for each transition in the last two columns of Table 4.

The accuracy of the computed transition parameters can also be estimated by comparisons with previous calculations and experiments. Figure 4 shows the comparison of our $\log(gf)$ values and the results from the NIST-ASD. Note that only the values in the NIST-ASD with uncertainties marked C and above are used for comparison. These NIST-ASD values are compiled by Wiese et al. (1996) and Wiese & Fuhr (2007) based on the results from Tachiev & Froese Fischer (2002), Musielok et al. (1995), and Hibbert et al. (1991). We can see that the agreement between our computed $\log(gf)$ results and the values from the NIST-ASD is rather good for most of the transitions.

In Figure 5 we compare our computed $\log(gf)$ values with the results from the other two calculations by Hibbert et al. (1991), performed with the CIV3 code, and by Tachiev & Froese Fischer (2002), using the MCHF-BP method. As is seen in the figure, the differences between the $\log(gf)$ values computed in this work and results from other sources are rather small for most of the transitions. When we compare our MCDHF/RCI results with those from the MCHF-BP calculations by Tachiev & Froese Fischer (2002), which are adopted in the NIST-ASD, 304 (261) out of 334 transitions are in agreement within 25% (10%). The exceptions are the weak transitions with $\log(gf) < -5$. Out of 305 transitions, 181 are in agreement within 25% with the results from Hibbert et al. (1991). It seems that when both theoretical results, i.e., those from Hibbert et al. (1991) and Tachiev & Froese Fischer (2002), are available for the transitions, our MCDHF/RCI results are in better agreement with the latter.

In Table 6, the computed transition probabilities are compared with the experimental results from Musielok et al. (1995) and Bridges & Wiese (2010). The theoretical results obtained from Hibbert et al. (1991) and Tachiev & Froese Fischer (2002), when available, are also listed for comparison. The estimated uncertainties dT of the MCDHF/RCI transition

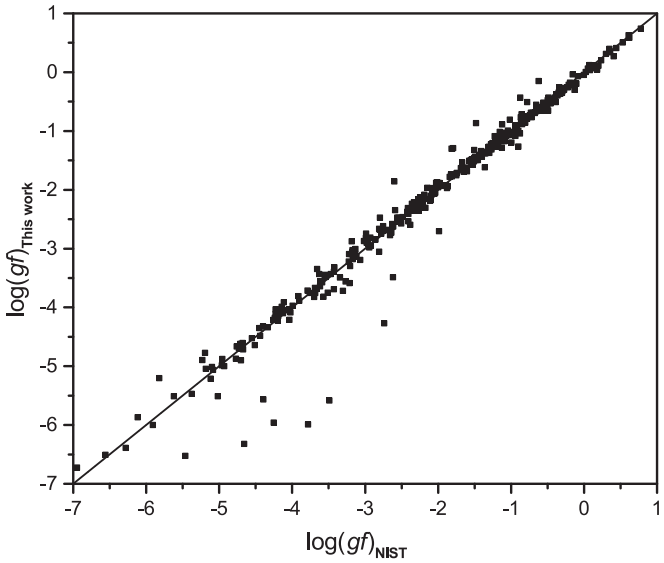

Figure 4. Comparison of the $\log(gf)$ values from our calculations with the results available in the NIST-ASD.

rates are given in parentheses. From Table 6 we can seen that when the two experimental results from Musielok et al. (1995) and Bridges & Wiese (2010) are both available for the multiplet, our results are in slightly better agreement with the latter for the $2p^2(^3P)3p \rightarrow 2p^2(^3P)3s$ transitions, while the situation becomes complex in the case of $2p^2(^3P)3d \rightarrow 2p^2(^3P)3p$ transitions. For the allowed $2p^2(^3P)3p \rightarrow 2p^2(^3P)3s$ transitions, our results are in excellent agreement with the two experimental results, as well as with the MCHF-BP (Tachiev & Froese Fischer 2002) and CIV3 (Hibbert et al. 1991) data. For the $2p^2(^3P)3d^4P \rightarrow 2p^2(^3P)3p^4D^o$ transitions, however, our results are in better agreement with the experimental values from Bridges & Wiese (2010) than with those from Musielok et al. (1995). For the transitions from the $2p^2(^3P)3d^4P_{5/2}$ and $^2F_{5/2}$ levels, the transition rates from our calculations differ substantially from the experimental values by Bridges & Wiese (2010), that is, by

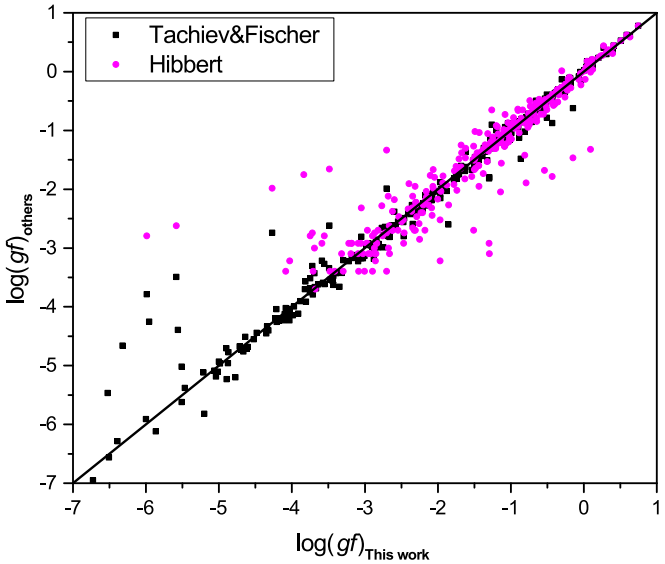

Figure 5. Comparison of the log(gf) values from our calculations with the values by Tachiev & Froese Fischer (2002) and Hibbert et al. (1991).

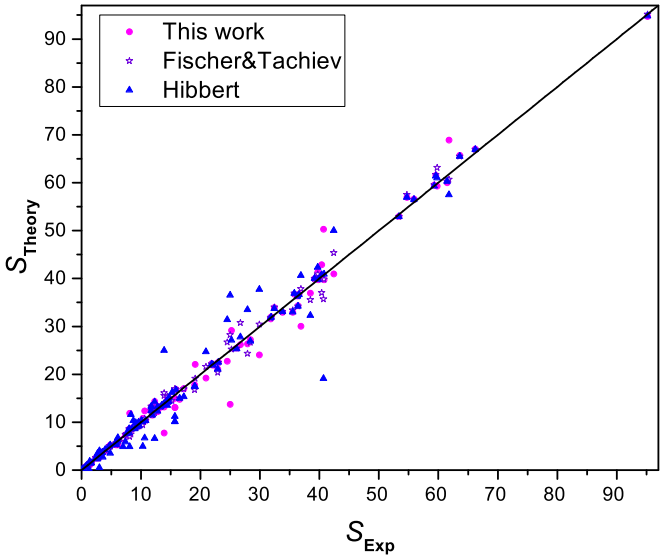

Figure 6. Comparison of the theoretical relative line strengths, S, with the corresponding experimental results published by Bacławski et al. (2002) and Bacławski & Musielok (2008).

70%, while the values from (Tachiev & Froese Fischer 2002) appear to be in better agreement with the corresponding experimental results. A closer inspection of the wave function composition given in Table 2 reveals a strong mixing between these two levels. It is very difficult to accurately calculate the radiative properties of such strongly interacting levels.

As can be seen from Table 6, when three theoretical values are available for the transitions, our MCDHF/RCI results seem to be in better agreement with the experimental values obtained by Musielok et al. (1995) than the others. Fifty out of 72 transitions from our calculations agree with Musielok et al. (1995) within 10%, while 33(37) out of 72 transitions are within the same range for the theoretical data from Hibbert et al. (1991; Tachiev & Froese Fischer 2002).

There are also a number of measurements of the line strength S. In Figure 6, the selected computed S values are compared with experimental results by Bacławski et al. (2002) and Bacławski & Musielok (2008). The theoretical results of Hibbert et al. (1991) and Froese Fischer & Tachiev (2004) are also shown in the figure. Note that Bacławski et al. (2002) and Bacławski & Musielok (2008) provided the relative line strengths within multiplets (normalized to 100). Therefore, all the theoretical values used for comparison in Figure 6 are fractions of the line strength for each transition in a multiplet, so that their sum is 100 for each multiplet. The computed S values from our work and the MCHF-BP calculations by Froese Fischer & Tachiev (2004) are in much better agreement with these experimental values than the CIV3 calculations by Hibbert et al. (1991). The S values from our work are within the uncertainties of the experimental measurements for most of the transitions.

3.3. Validation via the Solar Spectrum

The Sun is our best understood star, having well-constrained parameters (Prša et al. 2016), and for which both high-quality observations of the emergent intensity (Delbouille & Roland 1995; Neckel 1999; Doerr et al. 2016) and realistic simulations of the photospheric layer (Nordlund et al. 2009; Pereira et al. 2013) exist. As such, analyses of the solar intensity spectrum present an alternative way to test the accuracy of our calculations.

For this purpose, we consider the study of Amarsi et al. (2020). The authors presented a detailed analysis of five N I lines in the solar disk-center intensity spectrum, using state-of-the-art model atmospheres and radiative transfer methods. From this analysis, they measured for each line as well as for the average over all lines the solar nitrogen abundance, conventionally reported as the logarithmic number density of nitrogen nuclei relative to that of hydrogen nuclei (plus an offset): $A(\mathrm{N}) \equiv \log_{10}(N_{\mathrm{N}}/N_{\mathrm{H}}) + 12$. They adopted the transition probabilities given by Tachiev & Froese Fischer (2002). To first order, their results can be modified to account for new atomic data using

$$A(\mathrm{N})_{\mathrm{new}} = A(\mathrm{N})_{\mathrm{Tachiev}} + \Delta_{\mathrm{new}}, \quad (8)$$

where the correction term Δ_{new} is given by

$$\Delta_{\mathrm{new}} = \log(gf)_{\mathrm{Tachiev}} - \log(gf)_{\mathrm{new}}. \quad (9)$$

Table 7 presents the log(gf) values of the five permitted lines in N I used by Amarsi et al. (2020). The log(gf) values in both Coulomb and Babuskin forms from our calculations are given in the table. We can seen that for these five transition lines, our log(gf) values calculated in the Coulomb and Babuskin agree very well, with the dT values below 0.02. We also investigated the convergence of the wavelengths and oscillator strengths between the results from the calculations of the last two layers. The wavelengths have converged to within 0.1% for all the five transitions, and the difference between the oscillator strengths from the calculation of the last two layers is 0.0002 for 744.229 nm, 0.01 for 821.633 nm and 868.34 nm, 0.001 for 862.923 nm, and 0.005 for 1010.89 nm. Experimental measurements of transition probabilities for the lines were reported by Musielok et al. (1995) and Bridges & Wiese (2010); the derived log(gf) values are shown in the last two columns in Table 7. In all cases, our theoretical values and those from Tachiev & Froese Fischer (2002) fall into the range of the estimated uncertainties of the experimental values. The previous calculation by Hibbert et al. (1991) yielded higher

Table 6
Comparison of Transition Rates Obtained from Experimental Values with Our MCDHF/RCI and Other Calculations

Transition Array	Term	$g_u - g_l$	Transition Rate A (10^6 s^{-1})				
			MCDHF/RCI	Tachiev & Fischer[a]	Hibbert et al.[b]	Musielok et al.[c]	Bridges & Wiese[d]
$2p^2(^3P)3p - 2p^2(^3P)3s$	$^4D^o-^4P$	8-6	23.95(1.30%)	25.31(114)	25.96	22.1(24)	23.2(19)
		6-4	17.85(1.30%)	18.81(88)	19.25	16.7(18)	17.29(138)
		4-2	10.95(1.29%)	11.52(55)	11.79	10.4(11)	10.67(85)
		6-6	6.167(1.25%)	6.546(351)	6.725	5.95(71)	5.96(48)
		4-4	12.19(1.27%)	12.88(62)	13.20	11.7(13)	12.04(96)
		2-2	20.51(1.27%)	21.61(97)	22.11	19.7(22)	20.0(16)
		4-6	0.907(1.21%)	0.965(59)	0.993	0.88(12)	
		2-4	3.554(1.24%)	3.761(194)	3.857	3.24(39)	3.70(30)
$2p^2(^3P)3p - 2p^2(^3P)3s$	$^4P^o-^4P$	6-6	21.43(1.69%)	22.63(155)	23.07	22.1(27)	
		4-4	4.975(1.64%)	5.233(365)	5.312	5.02(60)	
		2-2	4.424(1.73%)	4.684(314)	4.771	4.85(58)	
		4-6	12.40(1.71%)	13.12(92)	13.41	13.4(16)	
		2-4	24.79(1.69%)	26.19(175)	26.67	26.5(32)	
		6-4	7.751(1.74%)	8.220(566)	8.385	7.86(94)	
		4-2	11.84(1.71%)	12.53(84)	12.74	12.2(15)	
$2p^2(^3P)3p - 2p^2(^3P)3s$	$^4S^o-^4P$	4-6	18.34(0.99%)	19.61(94)	20.17	19.0(21)	17.91(143)
		4-4	11.20(0.96%)	11.96(52)	12.36	12.3(14)	11.83(85)
		4-2	5.295(0.94%)	5.649(229)	5.856	5.63(62)	5.71(46)
$2p^2(^3P)3p - 2p^2(^3P)3s$	$^2D^o-^2P$	6-4	25.73(0.03%)	25.19(170)	26.79	25.5(31)	
		4-2	21.87(0.03%)	21.39(154)	22.63	21.9(26)	
		4-4	3.820(0.04%)	3.741(250)	4.043	3.88(50)	
$2p^2(^3P)3p - 2p^2(^3P)3s$	$^2P^o-^2P$	4-4	26.38(0.35%)	26.78(32)	27.52	25.2(30)	
		2-2	20.63(0.37%)	21.45(00)	21.58	19.8(24)	
		2-4	10.58(0.32%)	10.75(12)	11.08	9.70(116)	
		4-2	4.772(0.37%)	4.871(42)	5.106	4.64(60)	
$2p^2(^3P)4p - 2p^2(^3P)3s$	$^2P^o-^2P$	4-4	1.024(9.36%)			0.749(105)	
		2-2	0.895(9.61%)			0.672(94)	
		2-4	0.368(8.63%)			0.269(40)	
		4-2	0.207(9.67%)			0.240(36)	
$2p^2(^3P)3d - 2p^2(^3P)3p$	$^2P-^2S^o$	4-2	26.19(1.19%)	32.08(590)	32.72	28.7(37)	
		2-2	26.02(1.27%)	31.97(583)	32.65	30.0(39)	
$2p^2(^3P)4d - 2p^2(^3P)3p$	$^2P-^2S^o$	4-2	4.054(12.61%)			3.58(50)	
		2-2	4.221(12.95%)			3.64(51)	
$2p^2(^3P)3d - 2p^2(^3P)3p$	$^4F-^4D^o$	10-8	36.11(0.98%)	38.96(315)	39.05	37.5(49)	
		8-6	31.62(0.98%)	34.11(280)	34.17	31.9(42)	
		6-4	27.94(0.97%)	30.15(262)	30.17	28.5(37)	36.9(55)
		4-2	25.92(0.98%)	28.05(237)	27.94	26.2(34)	
		8-8	3.479(0.90%)	3.833(427)	3.991	3.97(52)	4.42(44)
		6-6	6.663(0.99%)	7.317(782)	7.606	7.31(95)	7.58(68)
		4-4	9.067(0.96%)	9.833(782)	9.936	9.89(129)	10.3(9)
		6-8	0.218(0.01%)	0.239(29)	0.237	0.326(46)	0.256(31)
		4-6	0.518(0.80%)	0.564(51)	0.579	0.413(58)	
$2p^2(^3P)3d - 2p^2(^3P)3p$	$^4P-^4D^o$	6-8	0.570(6.85%)	0.822(169)	0.668	1.39(18)	0.842(109)
		4-6	0.179(13.75%)	0.223(102)	0.048	0.450(63)	0.236(35)
		2-4	0.150(13.72%)	0.183(98)		0.311(44)	0.152(23)
		6-6	0.606(2.53%)	1.394(850)	2.471	2.28(30)	1.304(130)
		4-4	1.845(2.37%)	2.015(518)	2.787	3.64(47)	2.15(19)
		2-2	1.649(3.59%)	1.828(484)	2.999	2.93(38)	1.91(25)
		6-4	0.529(0.25%)	0.348(179)	0.332	0.760(106)	0.406(45)
		4-2	0.358(1.97%)	0.407(117)	0.707	0.758(106)	0.407(41)
$2p^2(^3P)3d - 2p^2(^3P)3p$	$^4D-^4D^o$	8-8	9.264(1.29%)	10.28(124)	10.02	8.82(115)	
		6-6	5.149(1.75%)	5.730(704)	4.900	4.79(62)	
		4-4	2.963(2.20%)	3.330(526)	2.408	2.99(39)	
		2-2	3.366(2.09%)	3.829(610)	2.640	3.22(42)	
		6-8	2.675(0.07%)	2.965(404)	3.243	2.58(34)	
		4-6	4.030(0.32%)	4.496(540)	4.717	4.10(53)	
		2-4	4.821(0.76%)	5.414(621)	5.603	4.77(62)	
		8-6	0.577(1.30%)	0.699(111)	0.751	0.534(75)	
		6-4	0.989(1.66%)	1.179(185)	1.115	1.09(14)	
		4-2	1.194(1.89%)	1.40(23)	1.151	1.16(15)	
$2p^2(^3P)3d - 2p^2(^3P)3p$	$^4P-^4P^o$	6-6	2.976(1.05%)	3.928(159)	3.069	2.37(31)	
		2-2	5.353(0.57%)	5.397(924)	9.480	3.39(44)	

Table 6
(Continued)

Transition Array	Term	$g_u - g_l$	Transition Rate A (10^6 s^{-1})				
			MCDHF/RCI	Tachiev & Fischer[a]	Hibbert et al.[b]	Musielok et al.[c]	Bridges & Wiese[d]
		4-6	3.721(0.79%)	3.757(363)	2.740	2.29(30)	
		2-4	6.649(0.89%)	6.751(701)	4.178	4.01(52)	
		6-4	4.829(0.65%)	7.16(160)	10.01	4.18(54)	
		4-2	8.942(0.70%)	9.027(793)	11.03	5.55(72)	
$2p^2(^3P)3d - 2p^2(^3P)3p$	$^4D-^4P^o$	8-6	24.10(0.27%)	25.46(66)	25.11	23.5(31)	
		6-4	12.38(0.18%)	13.20(80)	11.08	12.3(16)	
		4-2	6.058(0.10%)	6.541(706)	4.249	6.07(79)	
		6-6	11.88(0.43%)	12.35(66)	13.40	11.3(15)	
		4-4	15.14(0.36%)	15.91(42)	15.40	15.2(20)	
		2-2	17.97(0.25%)	19.11(120)	14.53	17.8(23)	
		4-6	3.254(0.48%)	3.332(347)	4.332	3.24(42)	
		2-4	7.305(0.42%)	7.553(747)	10.10	7.16(93)	
$2p^2(^3P)5s - 2p^2(^3P)3p$	$^4P-^4P^o$	6-6	1.811(8.10%)			1.75(25)	
		4-4	0.392(7.87%)			0.445(67)	
		2-2	0.348(7.72%)			0.365(55)	
		4-6	0.917(7.44%)			0.937(141)	
		2-4	1.838(7.46%)			1.94(29)	
		6-4	0.758(8.37%)			0.738(111)	
		4-2	1.019(8.08%)			0.979(147)	
$2p^2(^3P)5s - 2p^2(^3P)3p$	$^2P-^2D^o$	4-6	2.252(3.43%)			1.79(25)	
		2-4	3.086(7.70%)			2.85(40)	
		4-4	0.193(1.44%)			0.230(35)	
$2p^2(^3P)3d - 2p^2(^3P)3p$	$^2F-^4D^o$	6-6	1.719(0.57%)	1.064(481)	0.420	2.26(32)	1.34(16)
		8-6	0.595(1.00%)	0.609(331)	0.527	1.08(15)	0.646(78)
		6-4	0.268(2.32%)	0.485(687)	0.555	0.810(113)	0.462(55)
$2p^2(^3P)3d - 2p^2(^3P)3p$	$^2F-^4P^o$	6-4	3.564(0.62%)	1.289(1182)	0.160	1.03(14)	

Notes. Our values from the MCDHF/RCI calculations are given in the Babushkin gauge. The values in parentheses are the relative differences between the Babushkin and Coulomb gauges. Note that the values from the MCHF calculations are those compiled in the NIST database. The numbers in parentheses without a percent sign are the uncertainties with respect to the last digit quoted, for example, 25.31(114) implies 25.31 ± 1.14.
[a] Tachiev & Froese Fischer (2002).
[b] Hibbert et al. (1991).
[c] Musielok et al. (1995).
[d] Bridges & Wiese (2010).

log(gf) values than the experimental determinations for the 821.633 nm, 868.340 nm lines, while the recommended value for 868.340 nm line by Bautista et al. (2022) is slightly higher than the experimental results.

Figure 7 compares the data in Table 7 in terms of the solar nitrogen abundance using Equations (8) and (9). The upper panel compares the results based on our calculations with those based on the experimental measurements of both Musielok et al. (1995) and Bridges & Wiese (2010). We see that the mean solar nitrogen abundance from our calculations (in either gauge) agrees well with those from Musielok et al. (1995). Interestingly, this analysis reveals that the transition probability for the 1010.89 nm line from Bridges & Wiese (2010) is significantly overestimated, as it would imply a solar nitrogen abundance significantly lower than what is implied by the other N I lines.

The lower panel of Figure 7 compares the results based on our calculations with those based on the theoretical calculations of Tachiev & Froese Fischer (2002), Hibbert et al. (1991), and Bautista et al. (2022). We see that the mean solar nitrogen abundance from our calculations (in either gauge) is significantly higher than those from the other three data sets. In particular, this analysis suggests that the transition probability for the 868.340 nm line from Bautista et al. (2022) might be overestimated, as it would imply a solar nitrogen abundance significantly lower than what is implied by the other N I lines for all of the other theoretical transition probability data sets.

Our new calculations suggest $A(\mathrm{N}) = 7.79$ from the N I lines, with the results from both the Babushkin gauge and Coulomb gauge in agreement to 0.01 dex. This is an increase of 0.02 dex over the result from Amarsi et al. (2020) based on the transition probabilities given by Tachiev & Froese Fischer (2002). When the results from molecular lines ($A(\mathrm{N}) = 7.89$; Amarsi et al. 2021) are also factored in, our mean solar nitrogen abundance becomes 7.84, an increase of 0.01 dex over the result given in Asplund et al. (2021). The rather large difference between the abundances inferred from atomic and molecular lines discussed in Amarsi et al. (2021) is thus probably not caused by errors in the N I transition probabilities.

4. Conclusions

In the present work, MCDHF and complementary RCI calculations have been performed for the lowest 103 states of N I; extending the models of earlier state-of-the-art calculations. Excitation energies, lifetimes, wavelengths, line strengths, transition rates, and weighted oscillator strengths have been systematically computed and provided.

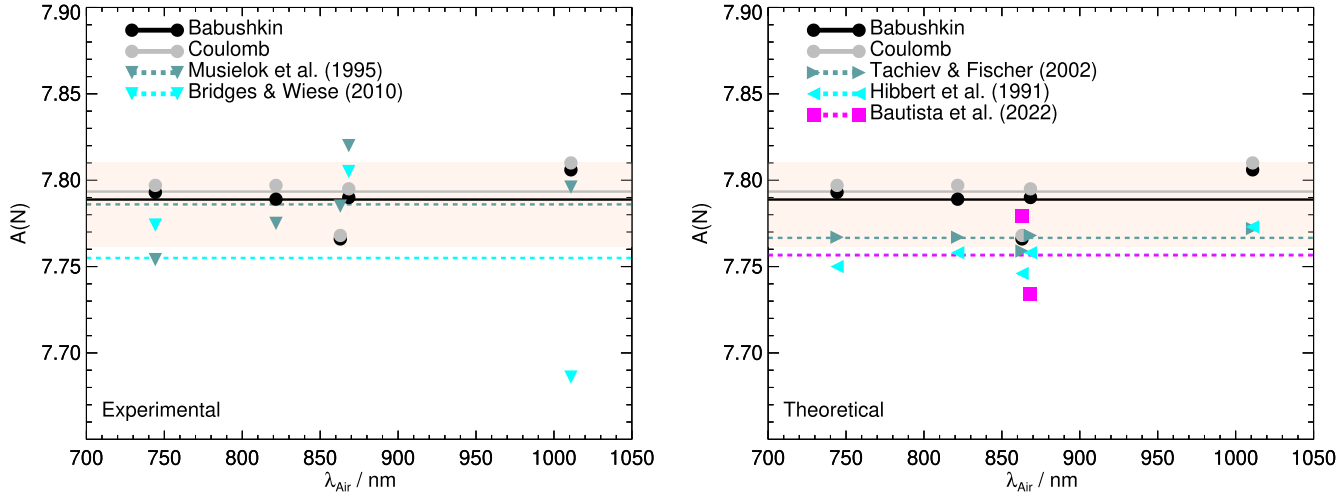

Figure 7. Solar nitrogen abundance inferred using different transition probabilities given in Table 7. The two panels illustrate the results based on the theoretical transition data computed in this work. The left panel also includes results based on the experimental data of Musielok et al. (1995) and Bridges & Wiese (2010), while the right panel includes results based on the theoretical data of Tachiev & Froese Fischer (2002), Hibbert et al. (1991), and Bautista et al. (2022). Horizontal lines show the mean abundance inferred from each data set. In both panels, the shaded region shows the standard deviation of the result based on the experimental data of Musielok et al. (1995), centered on the mean.

Table 7
Comparison of the log(*gf*) Values of the Five Lines Used for the Abundance Analysis in Amarsi et al. (2020)

Upper	Lower	λ_{air} (nm)	log(*gf*)						
			Our Values		Tachiev & Fischer[a]	Hibbert et al.[b]	Bautista et al.[c]	Musielok et al.[d]	Bridges & Wiese[e]
			B	C					
$2p^2(^3P)3p\,^4S^o_{3/2}$	$2p^2(^3P)3s\,^4P_{3/2}$	744.229	−0.429	−0.433	−0.403	−0.386		−0.39 ± 0.049	−0.41 ± 0.035
$2p^2(^3P)3p\,^4P^o_{5/2}$	$2p^2(^3P)3s\,^4P_{5/2}$	821.633	0.116	0.108	0.138	0.147		0.13 ± 0.053	
$2p^2(^3P)3p\,^2P^o_{3/2}$	$2p^2(^3P)3s\,^2P_{3/2}$	862.923	0.070	0.068	0.077	0.090	0.057 ± 0.046	0.051 ± 0.052	
$2p^2(^3P)3p\,^4D^o_{5/2}$	$2p^2(^3P)3s\,^4P_{3/2}$	868.340	0.084	0.079	0.106	0.116	0.14 ± 0.047	0.054 ± 0.047	0.069 ± 0.035
$2p^2(^3P)3d\,^4F_{5/2}$	$2p^2(^3P)3p\,^4D^o_{3/2}$	1010.89	0.410	0.406	0.444	0.443		0.42 ± 0.056	0.53 ± 0.065

Notes. The table lists upper and lower configurations along with their spectroscopic terms, wavelengths in air λ_{air}, and the weighted oscillator strength log(*gf*). B = Babuskin form and C = Coulomb form.
[a] Tachiev & Froese Fischer (2002).
[b] Hibbert et al. (1991).
[c] Bautista et al. (2022).
[d] Musielok et al. (1995).
[e] Bridges & Wiese (2010).

The comparison of the excitation energies with experimental data provided by NIST-ASD showed that the average relative differences of the computed energy levels are 0.07%. The accuracy of the transition data is evaluated based on the relative differences of the computed transition rates in the Coulomb and Babuskin forms, *dT*, and by extensive comparisons with previous theoretical and experimental results. A statistical analysis of the uncertainties *dT* of the E1 transitions is performed, and the mean *dT* for transitions with $A > 10^2$ s^{-1} is estimated to be 0.107 ($\sigma = 0.18$), and 0.045 ($\sigma = 0.08$) for transitions with $A > 10^6$ s^{-1}. The agreement of the experimental and our theoretical transition properties, for example, oscillator strengths, transition rates, and line strengths, is good overall. For some weaker transitions, however, e.g., intercombination transitions, significant discrepancies are present. These transitions are subject to strong cancellation effects and cannot be properly considered in our calculations. An improved method is needed to further decrease the uncertainties of the respective transition data.

In addition, our atomic data were employed in an analysis of the solar nitrogen abundance. Our new data suggest a mean solar nitrogen abundance $A(\mathrm{N}) = 7.79$ from five N I lines, with the results from both the Babushkin gauge and Coulomb gauge in agreement to 0.01 dex. The new abundance agrees well with that obtained from the experimental measurements of Musielok et al. (1995), but it is higher than those from the other theoretical data sets. However, a large difference between the abundances inferred from atomic and molecular lines (A(N) = 7.89, Amarsi et al. 2021) still exists, and it is probably not caused by errors in the N I transition probabilities.

M.C.L. would like to acknowledge the support from the Guangdong Basic and Applied Basic Research Foundation (2022A1515110043), the Professorial and Doctoral Scientific Research Foundation of Huizhou University No. 158020137. A.M.A. and J.G. gratefully acknowledge support from the Swedish Research Council (VR 2020-03940, 2020-05467). We

would also like to thank the anonymous referees for their useful comments that helped improve the original manuscript.

ORCID iDs

W. Li https://orcid.org/0000-0002-4569-1568
A. M. Amarsi https://orcid.org/0000-0002-3181-3413
J. Grumer https://orcid.org/0000-0002-6224-3492

References

Aerts, C., Molenberghs, G., Kenward, M. G., & Neiner, C. 2014, ApJ, 781, 88
Amarsi, A., Grevesse, N., Grumer, J., et al. 2020, A&A, 636, A120
Amarsi, A. M., Grevesse, N., Asplund, M., & Collet, R. 2021, A&A, 656, A113
Amarsi, A. M., Grevesse, N., Grumer, J., et al. 2020, A&A, 636, A120
Asplund, M., Amarsi, A., & Grevesse, N. 2021, A&A, 653, A141
Bacławski, A., & Musielok, J. 2008, JQSRT, 109, 2537
Bacławski, A., & Musielok, J. 2010, AcSpe, 65, 113
Bacławski, A., Wujec, T., & Musielok, J. 2002, PhyS, 65, 28
Bautista, M. A., Bergemann, M., Carvajal Gallego, H., et al. 2022, A&A, 665, A18
Belfiore, F., Maiolino, R., Tremonti, C., et al. 2017, MNRAS, 469, 151
Bengtsson, G., Larsson, J., Svanberg, S., & Wang, D. 1992, PhRvA, 45, 2712
Berry, H., Bickel, W., Bashkin, S., Désesquelles, J., & Schectman, R. 1971, JOSA, 61, 947
Bridges, J., & Wiese, W. 2010, PhRvA, 82, 024502
Bromander, J., Duric, N., Erman, P., & Larsson, M. 1978, PhyS, 17, 119
Catherinot, A., & Sy, A. 1979, PhRvA, 20, 1511
Copeland, R. A., Jeffries, J. B., Hickman, A. P., & Crosley, D. R. 1987, JChPh, 86, 4876
Cowan, R. D. 1981, The Theory of Atomic Structure and Spectra No. 3 (Berkeley, CA: Univ of California Press)
Delbouille, L., & Roland, C. 1995, in ASP Conf. Ser. 81, Laboratory and Astronomical High Resolution Spectra, ed. A. J. Sauval, R. Blomme, & N. Grevesse (San Francisco, CA: ASP), 32
Désesquelles, J. 1970, PhD Thesis, Lyon 1 Univ.
Doerr, H. P., Vitas, N., & Fabbian, D. 2016, A&A, 590, A118
Dumont, P., Biemont, E., & Grevesse, N. 1974, JQSRT, 14, 1127
Dyall, K., Grant, I., Johnson, C., Parpia, F., & Plummer, E. 1989, CoPhC, 55, 425
Ekman, J., Godefroid, M. R., & Hartman, H. 2014, Atoms, 2, 215
El-Sayed, F. 2021, JQSRT, 276, 107930
Esteban, C., Bresolin, F., García-Rojas, J., & Toribio San Cipriano, L. 2020, MNRAS, 491, 2137
Froese Fischer, C. 2009, PhST, T134, 014019
Froese Fischer, C., Gaigalas, G., Jönsson, P., & Bieroń, J. 2019, CoPhC, 237, 184
Froese Fischer, C., Godefroid, M., Brage, T., Jönsson, P., & Gaigalas, G. 2016, JPhB, 49, 182004
Froese Fischer, C., & Tachiev, G. 2004, ADNDT, 87, 1
Gaigalas, G., Froese Fischer, C., Rynkun, P., & Jönsson, P. 2017, Atoms, 5, 6
Gaigalas, G., Rynkun, P., Radžiute, L., et al. 2020, ApJS, 248, 13
Goldbach, C., Lüdtke, T., Martin, M., & Nollez, G. 1992, A&A, 266, 605
Goldbach, C., & Nollez, G. 1991, JPhy2, 1, C1
Grant, I. 1974, JPhB, 7, 1458
Grant, I. P. 2007, Relativistic Quantum Theory of Atoms and Molecules: Theory and Computation (New York: Springer)
Grevesse, N., Lambert, D. L., Sauval, A. J., et al. 1990, A&A, 232, 225
Hibbert, A., Biemont, E., Godefroid, M., & Vaeck, N. 1991, A&AS, 88, 505
Hirschi, R. 2007, A&A, 461, 571
Hutchison, R. B. 1971, JQSRT, 11, 81
Kolecki, J. R., & Wang, J. 2022, AJ, 164, 87
Kramida, A. 2013, FuST, 63, 313
Kramida, A. 2014, Atoms, 2, 86
Kramida, A., & Fuhr, J. 2010, NIST Atomic Transition Probability Bibliographic Database (v9.0) (Gaithersburg, MD: National Institute of Standards and Technology), doi:10.18434/T46C7N
Kramida, A., Ralchenko, Y., Reader, J. & NIST ASD Team 2021, NIST Atomic Spectra Database (v5.9) (Gaithersburg, MD: National Institute of Standards and Technology), https://physics.nist.gov/asd
Lambert, D. L. 1978, MNRAS, 182, 249
Lawrence, G., & Savage, B. D. 1966, PhRv, 141, 67
Li, W., Amarsi, A., Papoulia, A., Ekman, J., & Jönsson, P. 2021, MNRAS, 502, 3780
Maeder, A., Przybilla, N., Nieva, M.-F., et al. 2014, A&A, 565, A39
Mallow, J., & Burns, J. 1972, JQSRT, 12, 1081
Masseron, T., & Gilmore, G. 2015, MNRAS, 453, 1855
Musielok, J., Wiese, W. L., & Veres, G. 1995, PhRvA, 51, 3588
Neckel, H. 1999, SoPh, 184, 421
Nordlund, Å., Stein, R. F., & Asplund, M. 2009, LRSP, 6, 2
Olsen, J., Roos, B. O., Jo/rgensen, P., & Jensen, H. J. A. 1988, JChPh, 89, 2185
Papoulia, A., Ekman, J., Gaigalas, G., et al. 2019, Atoms, 7, 106
Pereira, T. M. D., Asplund, M., Collet, R., et al. 2013, A&A, 554, A118
Prša, A., Harmanec, P., Torres, G., et al. 2016, AJ, 152, 41
Przybilla, N., & Butler, K. 2001, A&A, 379, 955
Schiavon, R. P., Zamora, O., Carrera, R., et al. 2017, MNRAS, 465, 501
Smith, W. H., Bromander, J., Curtis, L., & Buchta, R. 1970, PhyS, 2, 211
Spite, M., Spite, F., Caffau, E., Bonifacio, P., & François, P. 2022, A&A, 667, A139
Sturesson, L., Jönsson, P., & Froese Fischer, C. 2007, CoPhC, 177, 539
Tachiev, G., & Froese Fischer, C. 2002, A&A, 385, 716
Takeda, Y., & Takada-Hidai, M. 1995, PASJ, 47, 169
Tong, M., Froese Fischer, C., & Sturesson, L. 1994, JPhB, 27, 4819
Vincenzo, F., & Kobayashi, C. 2018, MNRAS, 478, 155
Wiese, W. L., & Fuhr, J. R. 2007, JPCRD, 36, 1287
Wiese, W. L., Fuhr, J. R., Deters, T. M., et al. 1996, Atomic Transition Probabilities of Carbon, Nitrogen, and Oxygen: A Critical Data Compilation (Washington, DC: American Chemical Society), 157
Ynnerman, A., & Froese Fischer, C. 1995, PhRvA, 51, 2020